



Seismic swarms produced by rapid fluid injection into a low permeability laboratory fault

Sara Beth L. Cebry, Gregory C. McLaskey*

School of Civil and Environmental Engineering, Cornell University, Ithaca, NY, USA

ARTICLE INFO

Article history:

Received 29 May 2020

Received in revised form 14 December 2020

Accepted 16 December 2020

Available online xxxx

Editor: J.-P. Avouac

Keywords:

induced seismicity

fluid injection

earthquake initiation

heterogeneity

foreshock

laboratory experiments

ABSTRACT

Fluid injection, from activities such as wastewater disposal, hydraulic stimulation, or enhanced geothermal systems, decreases effective normal stress on faults and promotes slip. Earthquake nucleation models suggest the slip at low effective normal stress will be stable and aseismic—contrary to observed increases in seismicity that are often attributed to fluid injection. We conducted laboratory experiments using a biaxial loading apparatus that demonstrate how an increase in fluid pressure can induce “stick-slip” events along a preexisting saw-cut fault in a poly(methyl methacrylate) (PMMA) sample. We compared slip events generated by externally squeezing the sample (shear-triggered) to those due to direct fluid injection (fluid-triggered) and studied the effects of injection rate and stress levels. Shear-triggered slip events began on a localized nucleation patch and slip smoothly accelerated from slow and aseismic to fast and seismic. Fluid-triggered slip events initiated far more abruptly and were associated with swarms of tiny foreshocks. These foreshocks were able to bypass the smooth nucleation process and jump-start a mainshock resulting in an abrupt initiation. Analysis of these foreshocks indicates that the rapid injection of fluid into a low permeability fault promotes heterogeneous stress and strength which can cause many events to initiate—some of which grow large. We conclude that while a reduction in effective normal stress stabilizes fault slip, rapid fluid injection into a low permeability fault increases multi-scale stress/strength heterogeneities which can initiate small seismic events that have the potential to grow rapidly, even into low stress regions.

© 2020 Elsevier B.V. All rights reserved.

1. Introduction

Fluid injection for wastewater disposal, oil and gas operations, CO₂ sequestration, or enhanced geothermal systems (EGS) stimulates seismicity far from active tectonic regions (Ellsworth, 2013; Raleigh et al., 1976; Giardini, 2009). Mitigation of the seismic risk associated with various forms of fluid injection is a major consideration for these industries; however, the details of how fluid propagates along faults and potentially triggers earthquakes remain poorly understood. These operations strive to optimize permeability while minimizing the risk of induced seismicity. Doing so requires knowledge of fluid flow and pressure propagation, slip-dependent permeability changes, frictional changes, and how a fault can transition from aseismic to seismic slip (Amann et al., 2018).

Theoretical models present an apparent conflict between the effective stress law and earthquake nucleation models (Scuderi et al., 2017; Scuderi and Collettini, 2016). Effective stress law, which

is commonly thought to be the primary physical mechanism behind fault reactivation, demonstrates that when fluid is injected into a fault, the effective normal stress decreases, promoting fault slip (Noël et al., 2019; Segall and Rice, 1995). However, the stability of the induced slip—whether it is slow and aseismic or fast and seismic—is thought to be determined by nucleation models where an increase in fluid pressure favors stable and aseismic slip, rather than unstable and seismic slip events (Cappa et al., 2019; Scuderi and Collettini, 2018).

These predictions do not correlate simply to observations of induced seismicity. Injection has been found to induce aseismic slip (Cornet, 2016; Wei et al., 2015) which can trigger large seismic events. Earthquakes linked to wastewater disposal, such as those in Oklahoma, USA, can be large with $M = 5.7$ (Keranen et al., 2013) and/or come in swarms of smaller events $M < 4$ (Goebel and Brodsky, 2018). Hydraulic fracturing operations have also triggered large events $M > 4$ (Eyre et al., 2019). Seismic events have been linked to injection up to 35 km from the injection site and 18 yrs after the start of injection (Keranen et al., 2013, 2014). Swarms and aftershocks spread away from the injection site with time and are inferred to travel along existing faults.

* Corresponding author.

E-mail address: gcm8@cornell.edu (G.C. McLaskey).

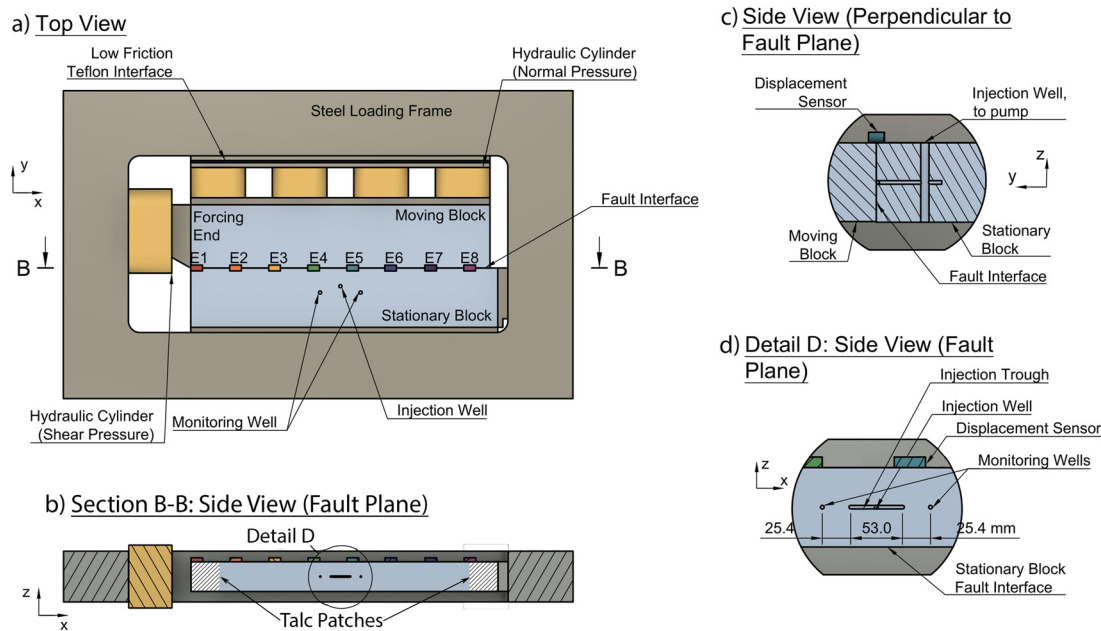


Fig. 1. Schematic of biaxial shearing apparatus and samples. (a) The sample, shown in light blue, consists of two 76 cm long clear PMMA forcing blocks. Pressure was applied to the samples with five hydraulic cylinders, shown in yellow. Eddy current displacement sensors (E1–E8) were placed along the fault to measure local fault slip. (b) A fault cross section showing that a light layer of talc gouge was put on the ends of the fault to allow the forcing and leading ends to creep rather than building up large stress concentrations. (c) Water was injected through a well in the stationary block to an injection trough cut in the fault interface. (d) Detail of the injection trough cut into the stationary-block side of the fault interface for fluid injection. Two holes were drilled 25.4 mm to either side of the injection trough on the stationary block and were used to monitor the fluid pressure on the fault at those locations. (For interpretation of the colors in the figure(s), the reader is referred to the web version of this article.)

In-situ studies support these observations and show seismic events directly correlated with fluid injection. Injection of fluids deep underground at Rangely oil field (Raleigh et al., 1976) and Rocky Mountain Arsenal (Healy et al., 1968), Colorado, USA confirmed that earthquakes can be triggered by an increase in fluid pressure with strong temporal correlation between the fluid pressure and seismic activity. More recent studies at shallow depth (<500 m) have found that seismic activity was a by-product of fluid induced aseismic slip (Guglielmi et al., 2014, 2015a; Cappa et al., 2019). While fluid injection does not systematically trigger earthquakes, controlling seismicity has proven non-trivial. At an EGS site in Helsinki, Finland, fluid injection was varied based on hydraulic and stored elastic energy balances to control stimulation-induced seismicity (Kwiatk et al., 2019). While seismicity was successfully kept below a project stopping criterion of M_w 2.0, 43,882 events $M_w > -0.5$ were catalogued over the 49 day simulation phase. Other EGS sites such as at Pohang and Basel have caused significant increases in seismicity leading to project shut-downs (Grigoli et al., 2018; Kim et al., 2018; Zastrow, 2019; Häring et al., 2008; Giardini, 2009).

Laboratory studies support the observation of fluid-induced seismic slip in velocity weakening materials (Bartlow et al., 2012; French et al., 2016; Noël et al., 2019; Passelègue et al., 2018) and aseismic slip, with seismicity as a by-product, in velocity strengthening materials (Scuderi and Collettini, 2018). While many studies demonstrate that unstable slip is possible, few studies address the theoretical nucleation model. Scuderi and Collettini (2018) explored this through experiments on shale fault gouge. They concluded that the fault gouge structure caused fluid to diffuse heterogeneously which caused accelerated, unstable slip.

This paper describes laboratory experiments of direct fluid injection onto a stressed, low permeability (fault diffusivity of 10^{-5} – 10^{-7} m²/s) fault with a focus on the nucleation process and associated seismicity. In the experiments, a plastic sample with a 760 mm long saw-cut simulated fault was deformed in a biaxial loading apparatus while water was injected directly into the center of the simulated fault through a hole drilled in the

sample (Fig. 1). During experiments, normal stress was held constant, while shear stress and water injection rate were varied to generate dynamic shear-triggered and fluid-triggered slip events. These dynamic “stick-slip” events are sudden episodes of rapid slip ($>10^{-3}$ m/s) that are thought to be analogous to earthquakes (Brace and Byerlee, 1966). Fluid injection was rapid relative to the fault diffusivity and sample dimensions such that high, localized overpressures built up on the fault.

This study builds upon previous laboratory and in-situ experiments by using a large laboratory fault (0.76 m) providing the ability to measure local phenomena. The nucleation and rupture patterns were monitored with eight displacement sensors and fluid pressure was recorded at three locations along the fault. In agreement with Passelègue et al. (2018), we found that increased injection rate caused a steeper pressure gradient along the fault. However, unlike previous laboratory experiments (Scuderi and Collettini, 2018) and shallow field studies (Guglielmi et al., 2015a,b), our fault length is large relative to the nucleation length scale. In our experiments, the nucleation process of the shear-triggered events involved a smooth acceleration of slip—from slow and aseismic to fast and fully seismic—on a localized region of the fault. The nucleation process of fluid-triggered events involved a larger region of slow slip (approximately twice that of shear-triggered slip) but initiated far more abruptly than in the shear triggered case. Swarms of tiny seismic events ($M - 6$ to $M - 4.5$) reminiscent of foreshocks accompanied fluid-triggered events but not shear-triggered events. We describe these seismic sequences as swarms because they contain many small events and lack a single, large event that is typical of foreshock-mainshock-aftershock sequences and standard stick-slip cycles. Instead, we often observed multiple sample-spanning dynamic rupture events without additional shear loading. This indicates that even after dynamic rupture, much of the fault remained at a stress level that was high enough to sustain another dynamic rupture that had initiated in the fluid-pressurized region.

We also found that some of the small seismic events, which we refer to as foreshocks, were able to bypass the nucleation process and abruptly transition into a complete-rupture stick-slip event.

We conclude that while reduced effective normal stress stabilizes a fault, fluid injection can, in many cases, increase multi-scale stress heterogeneities which counteract the stabilizing effects. The stress heterogeneities cause foreshocks, which are able to rapidly grow into large events. Rapid injection into a low-permeability fault promotes this type of behavior rather than slow aseismic slip.

2. Background

2.1. Effective stress law

Fault strength is commonly assumed to be proportional to effective normal stress (Hubbert and Rubey, 1959)

$$\sigma_{n, \text{effective}} = \sigma_n - P_f, \quad (1)$$

where σ_n refers to the normal stress on the fault and P_f refers to the pore pressure in the fault. Fluid injection increases P_f and reduces $\sigma_{n, \text{effective}}$. Faults slip when $\sigma_{n, \text{effective}}$, shear stress τ_s , and fault friction coefficient μ , reach a critical state defined by the Coulomb failure stress (Scholz, 2002)

$$CFS = \tau_s - \mu(\sigma_{n, \text{effective}}) > 0. \quad (2)$$

When $\sigma_{n, \text{effective}}$ is lowered, the fault is pushed closer to a critical state. However, in a fault with heterogeneous fluid diffusion, $\sigma_{n, \text{effective}}$ is only lowered where the fluid pressure is increased, not on the fault as a whole.

2.2. Nucleation length

Faults can slide in a manner that is stable and aseismic or unstable and seismic. Fault slip initiates following the effective stress law (Equation (2)). This initial slip is slow and stable until the slipping region grows to a critical nucleation length,

$$h^* \propto \frac{G * D_c}{\sigma_{n, \text{effective}}(b - a)}, \quad (3)$$

where G is the shear modulus of the fault material, D_c is the characteristic sliding distance, and $(b - a)$ is a rate and state friction parameter (Dieterich et al., 1992; Rice, 1993). While Equation (3) is described using rate and state parameters, similar expressions exist for linear slip weakening friction (e.g. Uenishi and Rice, 2003). When the size of the slipping patch reaches h^* , the fault slip accelerates into dynamic rupture. This process is referred to as earthquake nucleation. The rupture then propagates dynamically along the fault until unfavorable stress conditions are met, which cause the rupture to decelerate and terminate. If h^* is not reached, the fault remains stable and will continue to slide slowly. Effective stress law governs when a fault slips; nucleation conditions (Equation (3)) control whether the earthquake produced is slow and stable or fast and seismic.

In laboratory experiments, $h^* \approx 1$ m for bare granite/granite faults at $\sigma_{n, \text{effective}} \approx 8$ MPa (McLaskey, 2019). PMMA is more compliant ($G_{\text{granite}} \approx 30$ GPa, $G_{\text{PMMA}} \approx 2$ GPa), and estimated friction parameters of similar glassy polymers such as Homolite ($b - a = 0.005$, $D_c = 0.3\text{--}0.4$ μm (Lu, 2009) and polycarbonate ($b - a = 0.004$, $D_c = 0.2$ μm (Kaneko et al., 2016) result in $h^* \approx 10$ mm. Nucleation sizes of $h^* = 10\text{--}100$ mm have been observed (Nielsen et al., 2010; Guérin-Marthe et al., 2019) for polycarbonate at $\sigma_{n, \text{effective}} \approx 8$ MPa, and these estimates are generally consistent with our observations on PMMA.

3. Experimental methods

3.1. Apparatus and sample

Two PMMA forcing blocks were used in a direct shear biaxial apparatus shown in Fig. 1 (see McLaskey and Yamashita (2017) for additional apparatus details). The moving block is 760 mm by 203 mm by 76 mm (x, y, and z, as indicated in Fig. 1) and the stationary block is 790 mm by 152 mm by 76 mm (x, y, and z). These two blocks are collectively referred to as the sample. The simulated fault is a 760 mm by 76 mm interface in the x-z plane. The two PMMA surfaces that comprise the fault interface were machined flat and smooth then roughened with 80 grit abrasive. Biaxial experiments of this type typically have nonuniform $\sigma_n(x)$ with higher σ_n at the sample ends (Kammer et al., 2015; Ben-David et al., 2010b). In order to relieve the stress concentrations at the sample edges, a light layer of talc powder was placed on the fault 76 mm from the sample ends (see Fig. 1b). Talc is known to be velocity strengthening, so the above sample preparation allowed the sample ends to creep rather than build up large stress concentrations.

The two sample halves were pressed together using four hydraulic cylinders that apply a constant normal stress to the simulated fault in the y direction. Shear stress on the interface was applied by advancing a single hydraulic cylinder in the positive x direction using a high-performance liquid chromatography (HPLC) pump. A separate HPLC pump was used to inject water at a constant rate through a 3.5 mm diameter hole into an injection trough 53 mm long by 3.5 mm wide by 3 mm deep cut into the fault face of the stationary block. Two additional 3.5 mm diameter holes were drilled 25.4 mm from the edge of the injection trough in both the positive and negative x direction. These holes were used as monitoring wells to measure the water pressure on the fault at those locations. The top, bottom, and sides of the fault interface were left open to atmospheric pressure.

3.2. Instrumentation

Fluid pressures in the injection trough and monitoring wells were measured with 2 kPa and 1.3 kPa precision, respectively, using Omega PX309 series pressure transducers. Sample-average normal and shear stress on the fault were calculated from measured hydraulic pressure with precision of 3 kPa and 1 kPa, respectively. Eddy current displacement sensors were used to measure local fault slip along the top of the simulated fault at eight locations (E1-E8) as shown in Fig. 1. These sensors measure displacement to 0.15 micron, between a probe that was glued to the stationary block and a target glued to the moving block. Eight piezoelectric sensors (Panametrics V103, 13 mm diameter), used to measure vertical ground motions to within 12.5 μV , were glued on the moving block 30.0 mm from the fault in the y-direction. The four piezoelectric sensors on the top of the moving block were located 325, 375, 425, and 475 mm from the forcing end in the x-direction and those on the bottom were located 300, 350, 400, and 450 mm from the forcing end. Data from all sensors were recorded continuously at 50 kHz on a 20-channel digitizer then averaged to 5 kHz to reduce high-frequency noise. The piezoelectric sensor data was simultaneously recorded at 5 MHz in a triggered mode to capture the seismic events at higher temporal resolution.

3.3. Experimental procedure

Table 1 lists key variables for a suite of seven experiments reported here. All experiments were conducted by applying a sample-average normal stress, $\bar{\sigma}_n$, between 1 and 8 MPa, held

Table 1
Summary of experiments.

Exp. #	$\bar{\sigma}_n$ (MPa) Sample-average applied normal stress	R (mL/min) Water injection rate	$\bar{\tau}_{max}$ (MPa) Sample-average maximum shear stress	$max(\frac{\bar{\tau}_{max}}{\bar{\sigma}_n})$ Maximum sample average stress ratio	P_{max}^f (MPa) Maximum water pressure during injection	Mainshocks (#) Fluid-triggered slip events that ruptured the entire fault	Fore- and aftershocks (#) Fluid-triggered slip events that only ruptured part of the fault
1	7.6	5	3.0	0.39	8.7	2	20
2	0.85	10	0.47	0.54	2.4	2	3
3	0.88	5	0.49	0.54	2.2	2	3
4	0.85	1	0.50	0.55	1.6	0	1
5	7.7	5	3.1	0.39	8.6	3	24
6	0.90	3	0.46	0.50	2.1	2	2
7	0.96	2	0.51	0.52	2.1	2	1

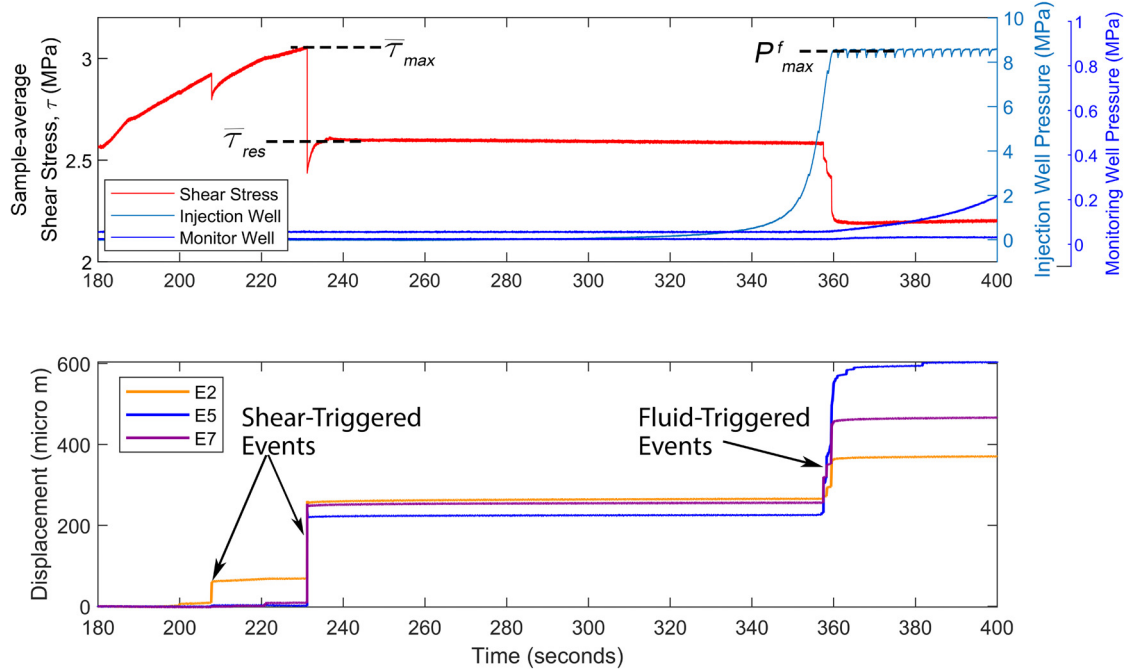


Fig. 2. Typical results from Experiment #5 ($\bar{\sigma}_n = 7.7$ MPa, $R = 5$ mL/min). The top graph shows the externally applied sample-average shear stress and fluid pressure at the injection well and two monitoring wells. $\bar{\tau}_{max}$ indicates the maximum sample-average shear stress the sample could sustain before slipping without fluid pressure. $\bar{\tau}_{res}$ indicates the residual stress after a shear-triggered slip event that ruptured the entire sample. P_{max}^f is the maximum fluid pressure measured at the injection well. $\bar{\sigma}_n$ was held constant at 7.7 MPa for the experiment. Fluid pressure oscillations are due to HPLC pump strokes. Monitoring wells showed only a tiny increase in pressure at the end of this time window. The lower graph presents the resulting slip measured at three locations along the fault. Two shear-triggered slip events were measured as indicated by the sudden changes in displacement and shear stress. A swarm of fluid-triggered slip events occurred later in the experiment as fluid pressure was increased.

constant for the duration of the experiment. In Phase I, sample-average shear stress, $\bar{\tau}$, was then increased by injecting hydraulic fluid at a rate of 0.167 mL/s resulting in a steady stress increase between 0.007 and 0.013 MPa/s until a slip event occurred. Events triggered solely by an application of externally applied shear stress without active fluid injection are referred to as “shear-triggered” events. $\bar{\tau}$ was increased until slip events occurred at regular time intervals at a consistent maximum sample-average shear stress level, $\bar{\tau}_{max}$ (Fig. 2). Maximum sample-average stress ratio, $\bar{\tau}_{max}/\bar{\sigma}_n$, ranged from approximately 0.39 to 0.55. At least three such slip events were generated during Phase I. Prior to the final shear-triggered slip event, we imposed a 90 s hold (by pausing the pump). Following the final shear-triggered slip event, the pump was paused again, such that shear pressure was held constant as close to the residual sample-average shear stress, $\bar{\tau}_{res}$, as possible, resulting in a sample-average stress ratio between 0.34 and 0.46. Then, during Phase II, water was injected directly into the fault at a prescribed rate, R , between 1 and 10 mL/min. Slip events that occurred due to an increase in fluid pressure are referred to as “fluid-triggered” events. Fluid pressure, P_f , measured at the point

of injection, ranged from 0 to 8.7 MPa. Experiments were conducted with water, apparatus, and samples at approximately 21 °C.

4. Results

4.1. Typical results

Fig. 2 shows results from Experiment #5 ($\bar{\sigma}_n = 7.7$ MPa, $R = 5$ mL/min), which is typical for experiments at higher $\bar{\sigma}_n$. At $t = 180$ s, $\bar{\tau}$ was increased after a 90-second hold. As $\bar{\tau}$ was increased, displacement sensors on the talc patches (E1 and E8, not shown in Fig. 2), showed that the talc patches slipped in episodic slow slip events reaching peak slip rates of around 10^{-4} m/s and creeping between events. Approximately once per shear event cycle, a faster, dynamic event propagated over 10 cm beyond the talc patch (Fig. 2, $t = 208$ s). We consider this event to be a shear-triggered foreshock. Throughout, we define dynamic events as those that radiated detectable seismic waves, and this roughly corresponds to slip rates $>10^{-3}$ m/s, and we refer to events that rupture the entire fault as mainshocks and partial-rupture events as foreshocks. Note that although mainshocks are always larger

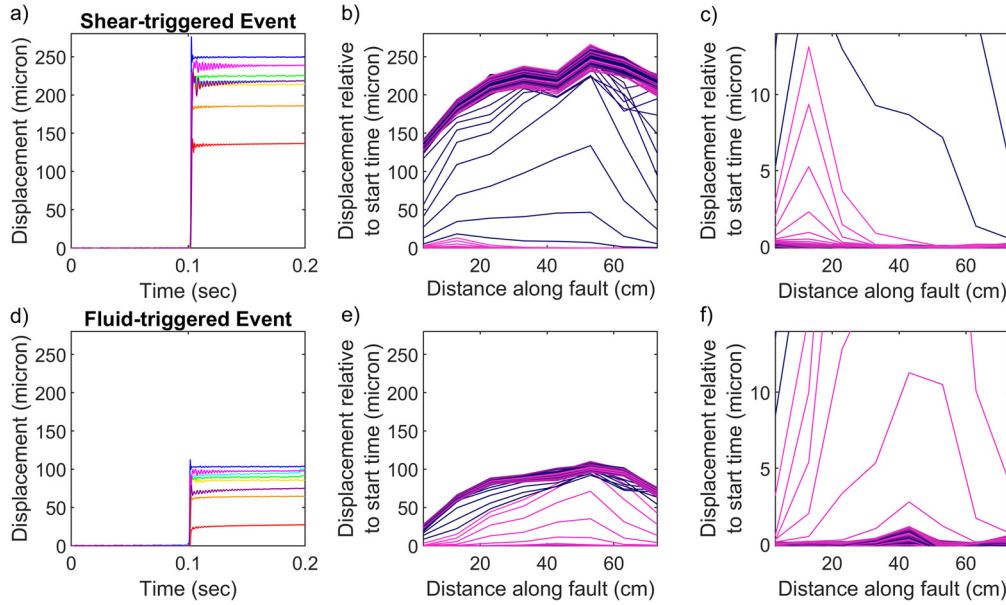


Fig. 3. Nucleation processes of a representative shear-triggered (a, b, c) and fluid-triggered (d, e, f) slip events from Experiment #5 ($\bar{\sigma}_n = 7.7$ MPa, $R = 5$ mL/min). Displacement sensor data for two of the slip events from the experiment in Fig. 2 displayed on the same time and displacement scale for comparison. (a, d) Local displacement measured by eight displacement sensors as a function of time. (b, e) Displacement as a function of distance along the fault shown by plotting a line showing slip along the fault every 100 μ s. The line colors cycle from light pink to dark purple every 5 ms, so that closely spaced lines that indicate slow fault slip appear as pink-purple banding. (c, f) Zoom in of (b) and (e) showing the nucleation of the shear-triggered event at $x = 10$ cm and the nucleation of the fluid-triggered event at $x = 45$ cm.

than foreshocks, their magnitude differences are far less than observed in the Earth. Since mainshocks ruptured the entire fault, their moment was limited by the finite size of the sample. We do not consider episodic slow slip events on the talc patches during shear loading to be foreshocks, only dynamic events that propagated 10 cm or more beyond the talc patch. During experiments conducted at $\bar{\sigma}_n \approx 1$ MPa, the talc patches crept without slow slip events, however we still observed one dynamic foreshock prior to some full slip events.

Fig. 2 shows a shear-triggered foreshock as indicated by the sudden 27 μ m increase in displacement on one or more displacement sensors at $t = 208$ s. And a second shear-triggered slip event, at $t = 231$ s ruptured the entire fault with an average slip of 105 μ m and will be referred to as a mainshock. $\bar{\tau}$ was then held constant near $\bar{\tau}_{res}$. Water was injected directly into the fault starting at 290 s. Fluid pressure measured in the injection well began to increase at 300 s and reached a maximum at 360 s. This triggered slip at the center of the fault (E5) starting at 355 s when $\bar{\tau} = 2.4$ MPa, $P_f = 4.8$ MPa. The fault continued to slip for an average of 158 μ m over 10 s in a series of three full (sample-spanning) and 24 partial (rupture does not span entire sample) dynamic slip events. An additional partial slip event occurred at $t = 382$ s, 17 s after the swarm of fluid-triggered events.

4.2. Comparison of shear-triggered and fluid-triggered slip events

Fig. 3 presents a representative shear-triggered, complete rupture, slip event from Experiment #5 that occurred at $t = 231$ s and a representative fluid-triggered, complete rupture, slip event that occurred at $t = 359$ s for comparison. The shear-triggered event was larger and slightly faster with slightly larger moment magnitude (210 μ m average displacement, 0.30 m/s, $M = -3.7$) than the fluid-triggered event (80.4 μ m, 0.12 m/s, $M = -4.0$). Fluid-triggered events occurred after the entire fault slipped, without reloading the applied shear stress (i.e. $\bar{\tau} \leq \bar{\tau}_{res}$). Shear-triggered mainshocks only occurred when applied shear stress reached $\bar{\tau}_{max}$.

Both mainshocks exhibited signs of slow slip in a region of the fault where dynamic rupture eventually initiated. We describe this region as the “nucleation patch” and define it as the region on the

fault where precursory slip exceeded 1 μ m/s in the 0.1 s prior to a dynamic slip event. This threshold is somewhat arbitrary and was chosen so that the nucleation patch would be clearly identified above the noise of our slip sensors. The properties of the nucleation patch were different for shear-triggered and fluid-triggered events. The fluid-triggered mainshock nucleated at the center of the sample where the fluid was injected and $\sigma_{n, effective}$ was lowest and its nucleation patch was somewhat larger (approximately 20 cm) than that of the shear-triggered mainshock (approximately 10 cm), which nucleated near the forcing end at the edge of the talc patch. The fluid-triggered event nucleated very slowly (1 μ m/s) for 1 μ m of slip before an abrupt initiation of dynamic rupture. For the shear-triggered event, slip on the nucleation patch gradually accelerated from slow slip at 10 μ m/s into dynamic rupture (slip rate ≈ 10 mm/s). There was some variability regarding the amount of slip prior to the dynamic slip event, however fluid-triggered events always initiated abruptly while shear-triggered events typically accelerated gradually.

4.3. Precursory seismicity

In addition to differences in nucleation measured by displacement sensors, shear- and fluid-triggered events differed with regards to precursory seismicity. Shear-triggered mainshocks were occasionally accompanied by one foreshock, as seen at $t = 208$ s in Fig. 2. Fluid-injection mainshocks were always accompanied by precursory slip, most commonly in the form of dynamic foreshocks. Fluid-triggered foreshocks initiated in the center of the sample, near the injection trough while shear-triggered foreshocks initiated near the forcing end. Fig. 4 and 5 show the slip, slip rate, and magnitudes of seismic events in a fluid-triggered swarm. Fig. 4 shows results from Experiment #5 ($\bar{\sigma}_n = 7.7$ MPa, $R = 5$ mL/min, also shown in Fig. 2 and Fig. 3). Fig. 5 shows results from Experiment #3 ($\bar{\sigma}_n = 0.88$ MPa, $R = 5$ mL/min). Most foreshocks ruptured to the top of the fault surface, but some only ruptured within the center of the fault (for example Fig. 4, $t = 355.5$ s). Those were not detected by the displacement sensors (and therefore do not have slip and slip rate information), but magnitudes were determined from piezoelectric sensor data. There are also

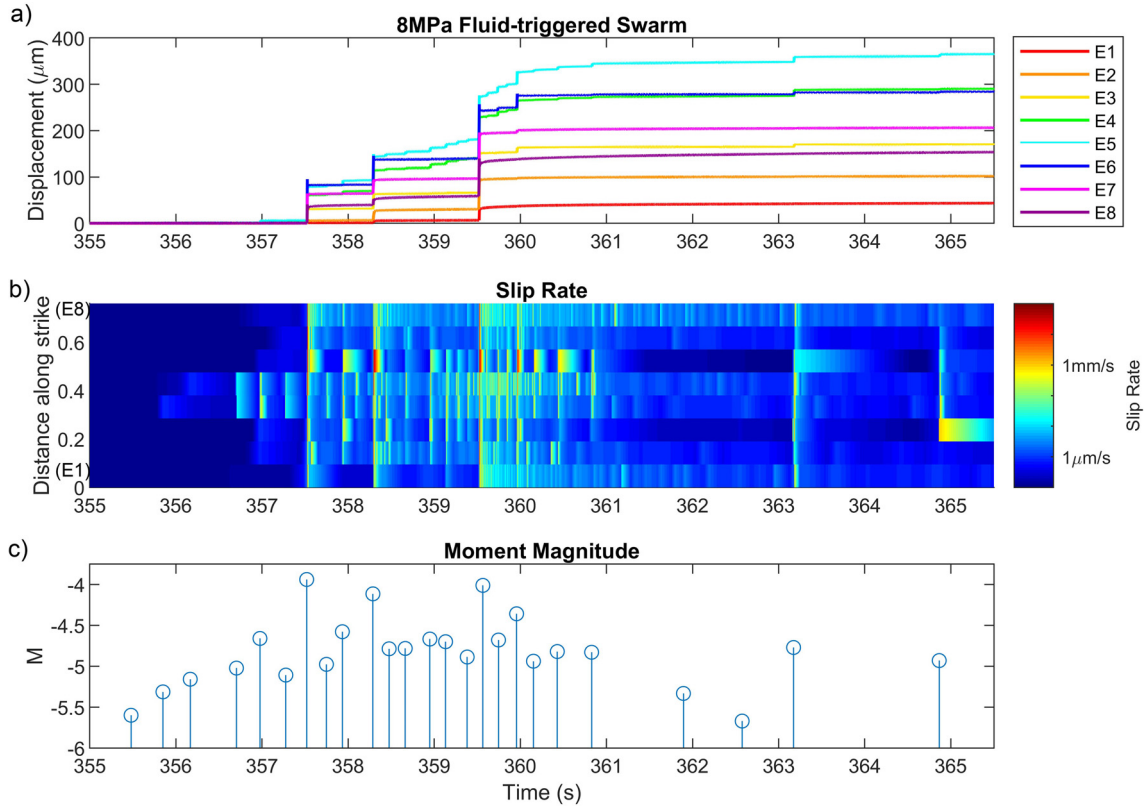


Fig. 4. Fluid-triggered sequence of 3 mainshock and 22 foreshock events from Experiment #5 ($\bar{\sigma}_n = 7.7$ MPa, $R = 5$ mL/min) also shown in Fig. 2. (a) The slip measured by the eddy current displacement sensors (E1–E8). (b) The slip rate derived from the displacement sensor data as a function of time and distance along the fault. (c) The magnitude of the slip events determined from ground motions measured by piezoelectric sensors. Some events were not captured by the displacement sensors on the top of the fault but were detected by the piezoelectric sensors.

cases of slow slip events that do not radiate detectable seismic waves but were detected via an increase in slip rate on displacement sensors (for example Fig. 5, $t = 270$ s).

Experiments at higher $\bar{\sigma}_n$ (#1, 5) resulted in at least six times more foreshocks than experiments at lower $\bar{\sigma}_n$ (#2, 3, 4, 6, 7). Experiments at low $\bar{\sigma}_n$ sometimes produced slow slip events (peak slip rate ≈ 6 μm/s) that did not radiate detectable seismic waves. No slow slip events were produced during experiments at high $\bar{\sigma}_n$. See Table 1 for a complete count of foreshocks and mainshocks in each experiment.

Foreshocks and mainshocks were also found to increase in number, speed, and magnitude with increasing injection rate, R . Experiments at high R (#3) resulted in two foreshocks and two mainshocks, while experiments at low R (#4) resulted in one small event that only ruptured a portion of the fault. Results from experiments at medium R (#6, 7) fell between these two end cases.

4.4. Calculation of moment magnitude

Vibrations detected by piezoelectric signals were used to calculate the moment magnitude of seismic events following a steel ball drop procedure described in McLaskey et al. (2015) and Wu and McLaskey (2019). Using a steel ball allowed us to calibrate the entire recording system (wave propagation, sensor response, and signal conditioning), rather than just the ground motions measured by the piezoelectric sensors. This method also allowed us to calibrate across a wide range of frequency bands (10^2 to 10^5 Hz) and convert from piezoelectric measurements directly to seismic moment. We characterize the spectra of earthquake sources using the amplitude of the Fourier transform of recorded time series. To obtain relative magnitudes, we compared the spectral amplitudes of different seismic events in the 1.5–3 kHz frequency band (red

squares and circles in Fig. 6). This frequency band was chosen because it had both good signal-to-noise ratio and was below the corner frequency of nearly all seismic events. (Complete-rupture events had lower corner frequencies and had to be analyzed in a lower frequency band.)

To determine the absolute magnitude of the seismic events, spectral amplitudes were compared to those of an empirical Green's function (EGF) event which was the impact of a 2.38 mm diameter steel ball dropped from 1 m onto the sample's top surface. The amplitude of the source spectrum of the ball impact at low frequencies is equal to the ball's change in momentum $\Delta p = 4.16 \times 10^{-4} \frac{\text{kg} \cdot \text{m}}{\text{s}}$, which we calculated from the mass of the ball (0.055 g) and its incoming and rebound velocities (4.43 m/s and -3.13 m/s). The ball source acts on the surface of the sample and has units of momentum (N·s) while the seismic events are internal and have units of moment rate (N·m/s). Internal and external sources can be related through the constant $C_{FM} = 4.14$ km/s, which is approximately equal to twice the average of the P- and S-wave velocities of the PMMA (McLaskey et al., 2015).

Fig. 6 shows the spectrum of the ball impact alongside the spectrum of a seismic event. Both spectra were computed from the Fourier transform of 0.1 ms segments of recorded ground motions centered on the first wave arrival. From this, we compute $\Delta\Omega$, the average (among four piezoelectric sensors) of the spectral differences between ball impact and seismic sources in the 1.5–3 kHz frequency band. This averaging over the different sensors produced more stable estimates of spectral differences with respect to directionality of the source and differences in source locations. Sensors located on the top of the sample were not used because of the strong Rayleigh waves excited by the ball that could bias the results (McLaskey et al., 2015). The seismic moment was calculated using $M_0 = \Delta\Omega * C_{FM} * \Delta p$ (McLaskey et

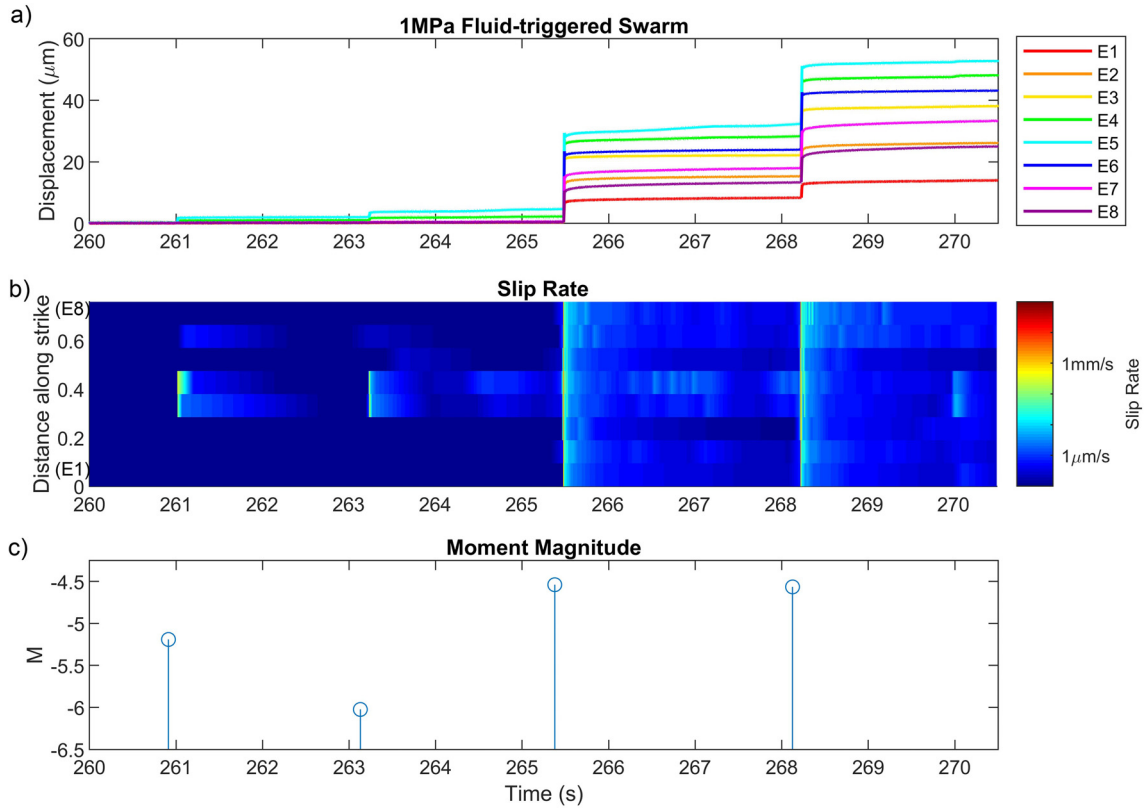


Fig. 5. Fluid-triggered sequence of 2 mainshock and 2 foreshock events from Experiment #3 ($\bar{\sigma}_n = 0.88$ MPa, $R = 5$ mL/min). (a) The slip measured by the eddy current displacement sensors (E1-E8). (b) The slip rate derived from the displacement sensor data as a function of time and distance along the fault. (c) The magnitude of the slip events determined from ground motions measured by piezoelectric sensors. One slip event ($t = 270$ s) was a slow slip event and any radiated seismic waves were not detected by piezoelectric sensors. This event was only detected by displacement sensors E4 and E5.

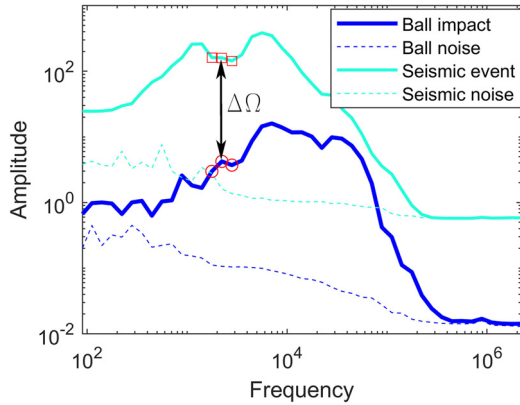


Fig. 6. Spectral comparison of a ball drop and a laboratory generated seismic event. Dark blue lines indicate the spectra from the ball impact. Light blue lines indicate the spectra from a fluid-triggered seismic event. Solid and dashed lines indicate the signal and noise respectively. Spectra were computed from the Fourier transform of 0.1 ms segments of recorded ground motions centered on the first wave arrival then averaged across the four piezoelectric sensors on the bottom of the sample. The noise spectra were derived from a signal of identical length captured before the first wave arrival. Red squares and circles indicate the frequencies used for comparison to determine the average spectral difference at low frequencies, $\Delta\Omega$.

al., 2015) and was then converted to magnitude using the relation $M_{Event} = \frac{2}{3} * \log(M_0) - 6.067$ (Hanks and Kanamori, 1979) defined for M_0 in units of N·m.

4.5. Seismic attributes of foreshocks and mainshocks

The initial ground motions of fluid-triggered foreshocks strongly resembled those of fluid-triggered mainshocks. Fig. 7 displays

piezoelectric sensor data from two collocated slip events: a mainshock from the experiment shown in Fig. 2 and the immediate preceding foreshock. This pair is presented as a representative example; all mainshocks from this experiment yielded similar results when compared with the preceding foreshocks. The initial 42–49 μs of signal from both sources are very similar. After 49 μs, the signals on all sensors diverged and the mainshock continued to grow about one order of magnitude while the foreshock remained the same or began to decay. Since the events were collocated, differences in the recorded seismograms were due to differences in the seismic source (fault rupture) rather than wave propagation effects. This comparison shows that the foreshock and mainshock ruptured in a similar manner (rupture area, slip amount, and slip rate) initially, before the mainshock grew into a $M -4.0$ event while the foreshock remained a $M -4.9$ event.

The comparison shown in Fig. 7 provides an opportunity to double check the consistency of the seismic and mechanical foreshock measurements. Assuming an average rupture velocity of about 1000 m/s (85% of the S-wave speed in PMMA), the 42–49 μs foreshock source duration equates to a rupture radius of about 4–5 cm. Consistent with this estimate, this foreshock was detected by only two displacement sensors spaced 10 cm apart. These instruments detected about $d = 2.5$ μm of slip, but were likely located near the edge of the slipped region, therefore we assume $d = 4$ μm is the average slip over the entire ruptured region. From the techniques outlined in Section 4.4, we used piezoelectric sensor measurements to determine the seismic moment $M_0 = 58.3$ N·m ($M -4.9$). From the measured seismic moment, the PMMA shear modulus $G \approx 2$ GPa, and the relation $M_0 = GAd$, we estimate the rupture area $A = 0.007$ m², corresponding to a radius of 5 cm, in good agreement with our mechanical estimate.

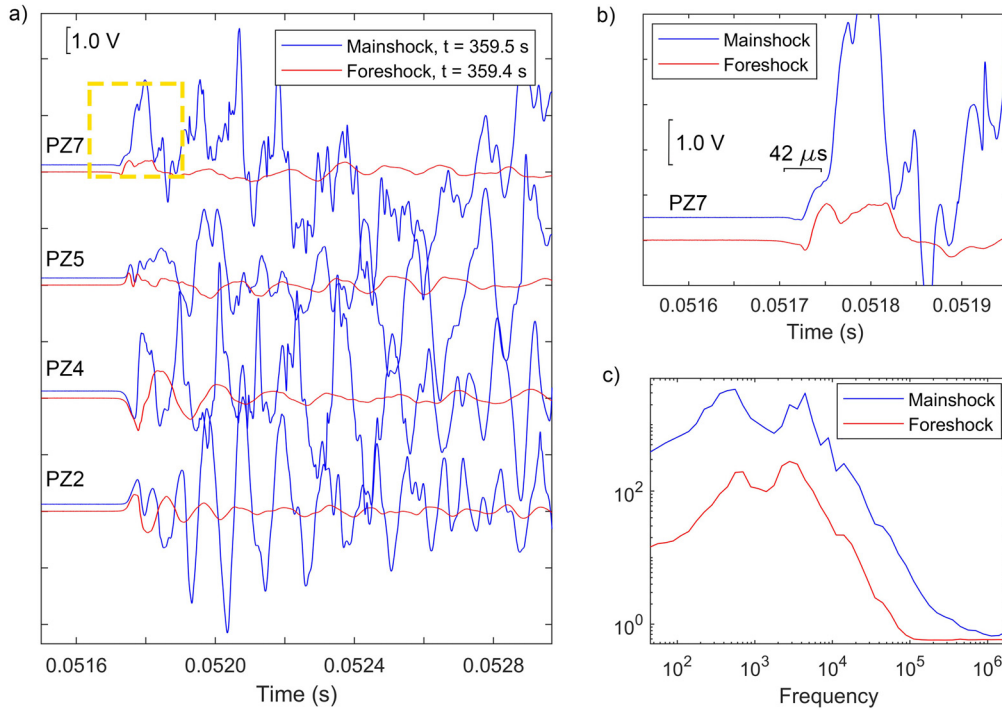


Fig. 7. Seismic waveforms of a fluid-triggered mainshock and the immediately preceding foreshock. (a) The waveforms, offset for clarity from four sensors. Two sensors were located close to the initiation point, PZ2 and PZ7, while two were located on opposite edges of the sensor array (PZ4 and PZ5). PZ2 and PZ4 were located on the top of the sample, PZ5 and PZ7 were located on the bottom of the sample. (b) Zoom in on the initiation of the waves from PZ7 as indicated by the yellow dashed box in (a). (c) shows the average spectra from all eight sensors.

5. Discussion

5.1. Hydraulic diffusivity of the fault

We used pressure measurements and a diffusion model to place bounds on the hydraulic diffusivity of the laboratory fault. During experiments, fluid pressure was measured in the injection well and in monitoring wells drilled 2.54 cm from the edges of the injection trough (Fig. 1d). A simple finite-difference model was created to match pressure measurements to diffusion parameters using a 1D diffusion equation, $\frac{\partial P}{\partial t} = \alpha \frac{\partial^2 P}{\partial x^2}$. In this equation, P is the fluid pressure and the hydraulic diffusion coefficient is $\alpha = \frac{k}{\beta_c \nu}$, where k is the fault permeability, β_c is the storage coefficient, and ν is the fluid's dynamic viscosity. Initial and boundary conditions in the model were set to match experimental measurements. Initially, the fluid pressure on the modeled fault was zero. After time zero, experimental pressure measurements made at the injection well were imposed as a boundary condition at the injection point in the model. Dirichlet boundary conditions were used at the edges of the fault, which were open to atmospheric pressure during the experiment.

Fig. 8a shows the 1D diffusion model, with the injection well, where the experimental fluid pressure measurements were imposed, the monitoring well, where numerical results were compared to experimental measurements, and the free surface at the end of the fault, which was left open to atmospheric pressure during the experiment. Fig. 8b compares the experimental measurements to numerical results for different modeled α . During the experiment, fluid was injected into the fault in the 10 s prior to the data window shown. These 10 s were presumably spent filling the trough and injection well before the injection pressure (solid blue line) began to noticeably increase at 0 s. After that, the pressure in the injection well increased rapidly and reached a steady state pressure of 5.8 MPa at 70 s. The pressure measured in the monitoring well (dotted orange line) increased very slowly at first (less

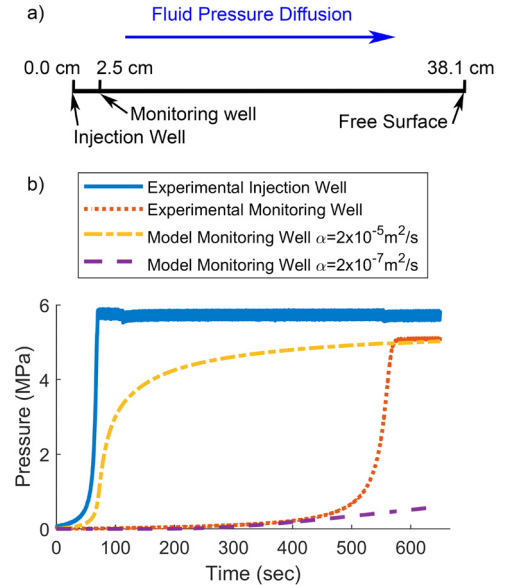


Fig. 8. 1D diffusion model to estimate diffusivity of fault. a) Schematic of the diffusion model showing the injection well where experimental injection well measurements were imposed, the monitoring well location where model results were compared to experimental measurements, and the free surface used to model the edge of the fault which was open to atmospheric pressure during the experiment. b) Typical results from fluid pressure measured at the monitoring well during fluid injection in an experiment with $\bar{\sigma}_n = 4$ MPa compared with a finite-difference model of fluid pressure diffusion using $\alpha = 2 \times 10^{-7} \text{ m}^2/\text{s}$ and $\alpha = 2 \times 10^{-5} \text{ m}^2/\text{s}$. One model matched the monitoring well measurements at short times, while another model better captured the steep change in pressure and maximum pressure observed at later times.

than 400 s) and later began to increase rapidly (at 500 s) before reaching a steady state pressure of 5.1 MPa at around 570 s.

The model with $\alpha = 2 \times 10^{-7} \text{ m}^2/\text{s}$ (dashed purple line) matched the monitoring well measurements for short term pres-

sure changes (<400 s from the start of fluid injection), while $\alpha = 2 \times 10^{-5}$ m²/s (dash-dot yellow line) accurately captured the steep change in pressure and maximum pressure of long term pressure changes from 550 s and on. It is likely that the permeability of the fault changed significantly as a function of pressure (Rutqvist and Stephansson, 2003), however this effect is neglected in the model. Due to the high compliance of PMMA, the fault was likely pried open during injection by the increased fluid pressure and this opened up pathways for the fluid to flow (Witherspoon et al., 1980). Fault roughness, which plays an important role in permeability for sheared faults (Ye and Ghassemi, 2018), was not considered and may have contributed to the permeability variance observed. The simple numerical model described above provided a means of bounding this problem; a more complex model is required to fully capture the coupled poromechanical behavior.

Additionally, there may have been small changes to permeability due to slip. While increased porosity during shearing may increase permeability of velocity strengthening gouges (Scuderi and Collettini, 2016), cumulative slip is considered to reduce permeability of granite faults (Bartlow et al., 2012). In some cases, a slight decrease in fluid pressure measured in the injection well occurred coincident with the largest stick-slip event of an experiment, indicating that the fault had increased permeability or dilated. Diffusivity is also affected by aseismic slip in front of and behind the pressure front (Cappa et al., 2018). However, these details are not considered in the diffusion model.

The modeling study above shows that the hydraulic diffusivity of the laboratory fault was relatively low—more consistent with previous studies of granite/granite faults under 50 to 200 MPa confining pressure, not faults in more permeable rocks like sandstones or poorly consolidated fault zones expected at shallow depths. Granite laboratory faults have been measured to have diffusion coefficients of 7.5×10^{-5} m²/s with permeabilities of 5×10^{-14} to 3×10^{-16} m² (Bartlow et al., 2012) and 7.895×10^{-17} m² (Kranz et al., 1979). However, in-situ pore pressure and slip measurements made at shallow depths implied fault diffusion coefficients of 4×10^{-2} m²/s with permeability values on the order of 10^{-12} m² (Bhattacharya and Viesca, 2019) orders of magnitude higher than the low permeability fault of our study.

5.2. Mechanics of foreshocks/precursors

Foreshocks are partial rupture events and require a heterogeneous distribution of stress and/or strength (Ke et al., 2018), so their existence provides insights into the spatial variation of fault stress/strength. First, they require a critically stressed fault patch larger than $h^* \approx 1$ to 10 cm (Nielsen et al., 2010; Guérin-Marthe et al., 2019), to initiate a dynamic rupture event, then the rupture must encounter unfavorable fault stress conditions to terminate before reaching the ends of the sample.

The solitary dynamic foreshock sometimes observed before shear triggered events ($t = 208$ s in Fig. 2) was similar to “precursors” observed in similar experiments on plastic samples (e.g. Rubinstein et al., 2007; Kammer et al., 2015). These “precursors” occurred because, during shear loading, the forcing end of the sample was highly stressed compared to the rest of the sample (see Fig. 2c, Bayart et al., 2018). Dynamic events nucleated in the highly stressed region, but the rest of the sample was only modestly stressed so the rupture terminated after propagating only a short distance. Those experiments exhibited sequences of precursors that progressively grew in size. Each event redistributed stress along the fault so that stress was reduced in the ruptured region and increased in the surrounding area which enabled the next slip event to propagate further (Ke et al., 2021; Ben-David et al., 2010a).

5.3. Fluid injection increases stress/strength heterogeneity

The steep fluid pressure gradient near the injection trough occurred because the fluid in the trough required time to diffuse away but the fluid injection rate was high. The hypocenters of fluid-triggered foreshocks were all located in the center of the sample, near the injection trough. Lowered $\bar{\sigma}_{n, effective}$ allowed earthquakes to nucleate there. Due to the steep pressure gradient and low sample-average shear stress (close to $\bar{\tau}_{res}$), those earthquakes quickly propagated into fault sections with low fluid pressure and higher $\bar{\sigma}_{n, effective}$. There they arrested and remained small foreshocks rather than throughgoing ruptures. Unlike shear-triggered events which had a maximum of one large, dynamic foreshock, multiple small fluid-triggered foreshocks were observed to occur before a slip event ruptured the entire fault. These observations indicate a far steeper gradient in stress was produced by fluid injection than by an increase in externally applied shear stress.

5.4. Effects of $\bar{\sigma}_n$ and injection rate

The number, size, and speed of fluid-triggered foreshocks increased with increasing $\bar{\sigma}_n$ and fluid injection rate, R . The dependence on $\bar{\sigma}_n$ is partly expected based on nucleation theory: h^* decreases with increasing $\bar{\sigma}_n$ (Equation (3)), and smaller h^* allows foreshocks to nucleate on smaller critically stressed patches. However, the dependence on R illustrates how fluid injection into a low permeability fault enhances stress/strength heterogeneities on multiple scales (Passelègue et al., 2018).

Fluid flowing on the fault interface is likely affected by μ m-sized features such as grooves, valleys, and dimples that exist on the fault surfaces. Detailed models that consider the fault roughness reveal that fluid flows along the fault interface in channels of different flow intensity, resulting in non-uniform stress (Shvarts and Yastrebov, 2018). The intensity of the stress/strength heterogeneity increases with decreasing permeability, as fluid is forced to flow along fewer and smaller channels. Increased σ_n decreases permeability (Kranz et al., 1979) and thus promotes heterogeneity and foreshocks. High injection rates also increase stress/strength heterogeneity because the fluid is unable to diffuse quickly enough to keep up with the rate at which it is injected. Passelègue et al. (2018) similarly found that fault reactivation was affected by rate of change of injection pressure, with higher rates of change resulting in significant pressure heterogeneities.

5.5. Foreshocks can initiate a large event

The initial seismic signatures of foreshocks were nearly identical to those of mainshocks. Fig. 7 shows an example of a foreshock-mainshock pair that occurred in the same location, 0.1 s apart, with the same initial seismic signatures. Fig. 4b and c show the spatial and temporal locations of events in the experiments with foreshocks occurring in the same location as mainshocks, less than 0.5 s prior to the mainshock. This indicates that the mainshocks and foreshocks begin as identical ruptures, but mainshocks encountered favorable rupture conditions and were able to propagate along the entire fault.

While the foreshock can initiate a large event, it is not a requirement in the nucleation process. Shear-triggered slip events initiated through a slow slipping nucleation patch that accelerated to initiate a mainshock without any immediate foreshocks. Fluid-triggered slip events exhibited a larger slow slipping nucleation patch, but also produced foreshocks, one of which eventually grew into a mainshock. This suggests that these events initiated in a combination of “preslip” and “cascade” nucleation models, similar to Fig. 15c of McLaskey (2019). It also suggests that critical

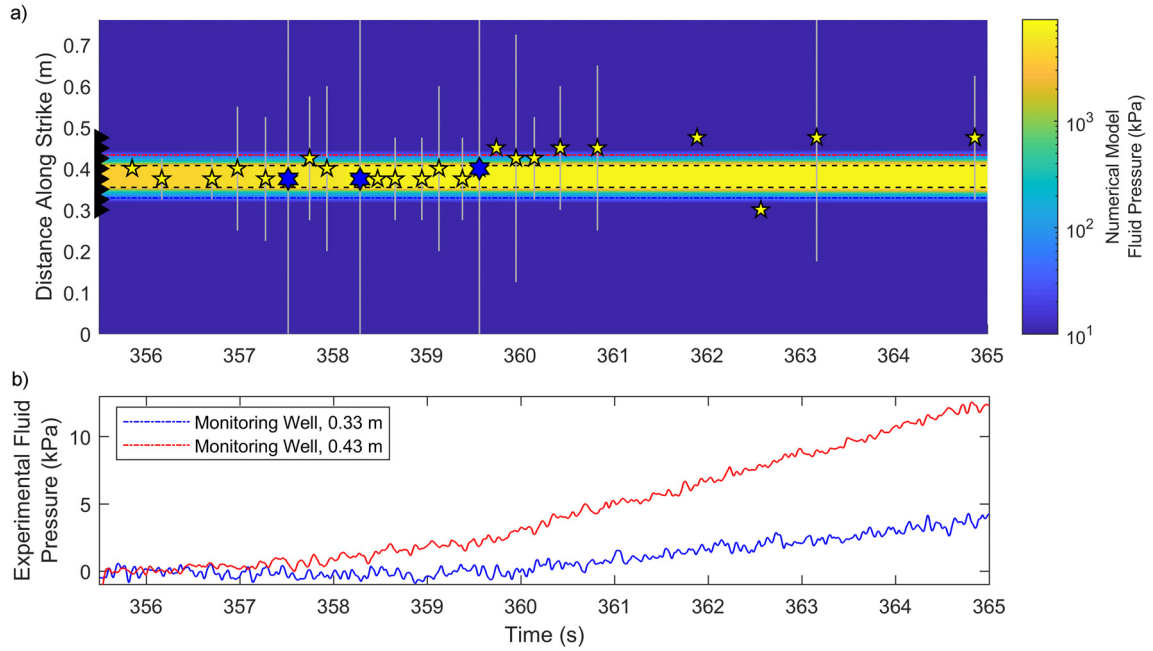


Fig. 9. Event hypocenters on a fluid pressure map. (a) Fluid pressure as a function of time and distance along the strike of the fault. Colors indicate fluid pressure and are on a log scale from 10 kPa (the pressurized zone) to 9 MPa (the maximum pressure during the experiment). Fluid pressure is determined by a simple 1D diffusion model. This model uses $\alpha = 1 \times 10^{-6} \text{ m}^2/\text{s}$, an appropriate diffusivity for this point in the experiment (see Section 5.1 for more details). Yellow 5-pointed stars indicate foreshock hypocenter locations. Blue 6-pointed stars indicate mainshock hypocenter locations. Seismic event hypocenter locations were approximated by determining the piezoelectric sensor (locations along strike indicated by black triangles on the left) to receive the earliest first wave arrival. Vertical gray lines indicate the rupture extent. Dashed black horizontal lines indicate the extent of the injection trough. Dashed-dot red and blue lines indicate the location of monitoring wells. (b) Fluid pressure measured at the monitoring wells during the experiment. Monitoring well data was used to constrain the numerical model.

nucleation length is not the only metric needed to characterize earthquake initiation, since a foreshock can jumpstart a mainshock in a process referred to as “cascade up” (Noda et al., 2013). Factors that influence stress heterogeneities on the fault, particularly injection rate and diffusivity, will have a direct effect on foreshocks, and therefore are important metrics in characterizing induced earthquakes initiation (Passelègue et al., 2018).

5.6. Slip outpaces fluid pressure

Fig. 9a compares the model-estimated fluid pressure in space and time alongside the hypocenter locations of the 24 foreshocks and mainshocks shown in Fig. 2 and Fig. 4. The 1D model best represents the pressure halfway through the thickness of the sample where pressure was the greatest during experiments (see Section 5.1). The model also uses $\alpha = 1 \times 10^{-6} \text{ m}^2/\text{s}$, appropriate for 65 to 75 s from the start of injection.

Due to the low permeability of the laboratory fault, fluid pressure on most of the fault was less than 10 kPa during experiments, three orders of magnitude smaller than $\bar{\sigma}_n$. We define the area of the fault with fluid pressure greater than 10 kPa as the “pressurized zone.” It took approximately one minute after the start of fluid injection for the pressurized zone to expand to the location of the monitoring wells only 25.4 mm away (Fig. 9b). In almost every seismic event (foreshocks and mainshocks), slip extended far beyond the pressurized zone as indicated by the gray vertical lines in Fig. 9a. For most experiments, both seismic slip during events and aseismic slip between events was measured by displacement sensors located along the top of the fault, at least 38 mm from the injection trough and clearly outside the pressurized zone, similar to results of more complex hydromechanical models (Bhattacharya and Viesca, 2019; Cappa et al., 2018; Wynants-Morel et al., 2020). Additionally, the complete rupture events clearly show that a fluid-triggered earthquake can rupture an area that is at least an order of magnitude larger than the pressurized area.

The propagation of dynamic rupture from inside the pressurized zone to the entire sample where $\bar{\tau} \leq \bar{\tau}_{res}$ illustrates how fault conditions needed to sustain a propagating rupture differ greatly from those needed to initiate it. Before fluid injection, $\bar{\tau} \leq \bar{\tau}_{res}$. When fluid was injected, pore pressure increased locally, but the rupture propagated far into regions without significant changes in fluid pressure. These areas, which would never initiate a seismic event on their own, and may therefore be labeled a low stress environment, were still able to sustain the rupture all the way to the sample ends.

5.7. Comparison to natural earthquakes

The nucleation process of natural earthquakes is not currently observable, but seismicity patterns in our experiments show some similarities to fluid-induced seismicity seen in the Earth. First, we observe fluid induced swarms consisting of many small foreshocks and a few larger mainshocks. This is similar to natural induced earthquakes which occur in swarms and often include one or more large dynamic events (Martínez-Garzón et al., 2014; Wei et al., 2015; Hauksson et al., 2013). Second, in our experiments we see that seismicity can occur with $\bar{\tau} < \bar{\tau}_{res}$. In the Earth, we see that seismicity can be induced in areas with low seismicity prior to fluid injection (Keranen et al., 2014). Finally, similar to our experiments, swarms of seismicity were found to outpace fluid pressure and/or occur where changes in fluid pressure are assumed to be very small (Goebel and Brodsky, 2018; Bhattacharya and Viesca, 2019).

Our experiments involved direct fluid injection into a low permeability fault cut in an impermeable PMMA sample. Results from these experiments are applicable to low permeability faults in low permeability rock masses, such as shale formations, commonly targeted for hydraulic fracture operations, or faults in the crystalline basement, where many fluid-induced earthquakes are known to initiate. Rapid fluid injection into low permeability faults promote

stress heterogeneities, since fluids take longer to diffuse away. Slower fluid injection into higher permeability faults or more permeable host rocks will experience different behavior: fluid is able to diffuse more rapidly, so stress changes associated with fluid injection are smoother and are applied more uniformly over a larger fault area. In a highly permeable fault, foreshocks would not be expected close to the injection point. Instead, seismic events would most likely occur on near-critically stressed faults that are nudged to failure by the fluid pressure. The nucleation processes and seismicity patterns of those fluid-triggered earthquakes would be harder to distinguish from natural earthquakes that are not associated with fluid injection.

In many of our experiments, P_{max}^f (measured in the injection well) $\geq \sigma_n$, which is not typically expected in the Earth. Nevertheless, we expect many aspects of the fluid-earthquake interactions described here are similar to processes taking place in the Earth at somewhat higher $\sigma_{n, effective}$. The low permeability of the laboratory fault is a contributing factor in the build-up of over pressure at the injection well. Neuzil (1995) proposed that abnormal pressures in the Earth occur when $\frac{L*\Gamma}{k} > 1$, where k is the permeability, L is the distance from the fluid source or sink to the nearest boundary condition, and Γ is the geologic forcing of fluid within rocks and can be thought of as analogous to the water injection rate in our experiments. While the analogy from the Earth to the laboratory is not perfect, the high pressures in our laboratory experiments are expected on a low permeability fault with the nearest boundary far away relative to the high injection rate.

During our experiments, the fluid pressure in the injection well eventually reached a steady state pressure P_{max}^f . This resulted from fluid escaping out the sides of the fault, which were open to atmospheric pressure. This can be seen in Fig. 2, at around 370 s. Once P_{max}^f was achieved, the top and bottom of the fault leaked significantly, however, despite this “short circuit” some fluid continued to spread along the fault since pressure at the monitoring wells did not reach a steady state pressure until 10 to 30 min later. While cracks in the Earth are not open to atmospheric pressure, permeability of the Earth is not constant, and close proximity to a high permeability pathway may produce similar conditions.

6. Conclusions

Fluid injected directly onto a fault decreases $\sigma_{n, effective}$ which promotes slip. Earthquake nucleation theory suggests that low $\sigma_{n, effective}$ could increase the critical nucleation length h^* , which would help stabilize fault slip so that it occurs slowly and mostly aseismically rather than fast and dynamically. We conducted a suite of laboratory experiments designed to explore these mechanical and seismic interactions and compare fluid-triggered slip events to those triggered by externally applied shear stress without fluid pressure. We found that decreased $\sigma_{n, effective}$ through fluid injection did allow for a larger region of slow and stable fault creep, which could be interpreted as a large h^* . Despite this, we observed that fluid-triggered dynamic rupture initiated more abruptly than in similar cases without fluid injection. The reason for this is that fluid injection also increased the heterogeneity of the $\sigma_{n, effective}(x)$, which promoted swarms of tiny seismic events (foreshocks), and allowed dynamic rupture to initiate abruptly in a “cascade up” process (e.g. Noda et al., 2013; McLaskey, 2019). The initial P-wave signatures of small and large seismic events were identical, and this indicates that the small foreshocks can grow rapidly into large seismic events if they encounter on-fault stress conditions that are favorable for rupture. Our experiments highlight that faults with relatively low average stress levels, that are unable to initiate slip, can still be favorable (enough) to sustain dynamic rupture that initiated elsewhere. Fluid injection into a low

permeability fault creates a localized, highly stressed region where dynamic rupture events can initiate and potentially propagate.

The results described above are likely applicable to rapid fluid injection into relatively low permeability faults. In such a case, fluid flows primarily along a few pathways and this sets up a strongly heterogeneous distribution of $\sigma_{n, effective}$ —ideal conditions for the generation of swarms of seismic events. When fluid is injected slowly or into a high permeability formation, there is time for fluid pressure to diffuse and smooth the stress field. Supporting this conclusion, we found that the number of foreshocks observed in our experiments increased both with increasing normal stress (which decreased permeability) and increasing injection rate.

Theoretical models of earthquake nucleation typically assume homogeneous $\sigma_{n, effective}$ which may lead to inaccurate predictions under fluid injection scenarios. We conclude that while the nucleation length may increase under fluid-injection conditions, the increased stress heterogeneity counteracts any stabilizing effects. Fluid injection produces swarms of small seismic events that, in some cases, can grow rapidly into a large dynamic event that propagates far outside the pressurized region.

CRedit authorship contribution statement

Sara Beth L. Cebry: Data curation, Formal analysis, Investigation, Methodology, Visualization, Writing – original draft, Writing – review & editing. **Gregory C. McLaskey:** Conceptualization, Formal analysis, Funding acquisition, Resources, Supervision, Writing – review & editing.

Declaration of competing interest

The authors declare that they have no known competing financial interests or personal relationships that could have appeared to influence the work reported in this paper.

Acknowledgements

We thank editors Miaki Ishii and Jean-Philippe Avouac and three anonymous reviewers whose comments helped improve this paper. This work was supported by National Science Foundation Grant EAR-1847139. Data used in this paper were acquired during laboratory experiments conducted at Cornell University. Data reported here are publicly available online at <https://doi.org/10.7298/enph-mx14>.

References

- Amann, F., Gischig, V., Evans, K., Doetsch, J., Jalali, R., Valley, B., et al., 2018. The seismo-hydromechanical behavior during deep geothermal reservoir stimulations: open questions tackled in a decimeter-scale in situ stimulation experiment. *Solid Earth* 9 (1), 115–137. <https://doi.org/10.5194/se-9-115-2018>.
- Bartlow, N., Lockner, D., Beeler, N., 2012. Laboratory triggering of stick-slip events by oscillatory loading in the presence of pore fluid with implications for physics of tectonic tremor. *J. Geophys. Res., Solid Earth* 117 (B11). <https://doi.org/10.1029/2012JB009452>.
- Bayart, E., Svetlizky, I., Fineberg, J., 2018. Rupture dynamics of heterogeneous frictional interfaces. *J. Geophys. Res., Solid Earth* 123 (5), 3828–3848. <https://doi.org/10.1002/2018JB015509>.
- Ben-David, O., Cohen, G., Fineberg, J., 2010a. Short-time dynamics of frictional strength in dry friction. *Tribol. Lett.* 39, 235–245. <https://doi.org/10.1007/s11249-010-9601-9>.
- Ben-David, O., Rubinstein, S., Fineberg, J., 2010b. Slip-stick and the evolution of frictional strength. *Nature* 463 (7277), 76–79. <https://doi.org/10.1038/nature08676>.
- Bhattacharya, P., Viesca, R., 2019. Fluid-induced aseismic fault slip outpaces pore-fluid migration. *Science* 364 (6439), 464–468. <https://doi.org/10.1126/science.aaw7354>.
- Brace, W., Byerlee, J., 1966. Stick-slip as a mechanism for earthquakes. *Science* 153 (3739), 990–992. <https://doi.org/10.1126/science.153.3739.990>.
- Cappa, F., Guglielmi, Y., Nussbaum, C., Birkholzer, J., 2018. On the relationship between fault permeability increases, induced stress perturbation, and the growth

- of aseismic slip during fluid injection. *Geophys. Res. Lett.* 45 (20), 11,012–11,020. <https://doi.org/10.1029/2018GL080233>.
- Cappa, F., Scuderi, M., Collettini, C., Guglielmi, Y., Avouac, J.-P., 2019. Stabilization of fault slip by fluid injection in the laboratory and in situ. *Sci. Adv.* 5. <https://doi.org/10.1126/sciadv.aau4065>.
- Cornet, F., 2016. Seismic and aseismic motions generated by fluid injections. *Geomech. Energy Environ.* 5, 42–54. <https://doi.org/10.1016/j.gete.2015.12.003>.
- Dieterich, J., Aki, K., Ohnaka, M., Ruff, L., Spudich, P., 1992. Earthquake nucleation on faults with rate- and state-dependent strength. *Tectonophysics* 211, 115–134. [https://doi.org/10.1016/0040-1951\(92\)90055-B](https://doi.org/10.1016/0040-1951(92)90055-B).
- Ellsworth, W., 2013. Injection-induced earthquakes. *Science* 341, 1–7. <https://doi.org/10.1126/science.1225942>.
- Eyre, T., Eaton, D., Zecevic, M., D'Amico, D., Kolos, D., 2019. Microseismicity reveals fault activation before Mw 4.1 hydraulic-fracturing induced earthquake. *Geophys. J. Int.* 218 (1), 534–546. <https://doi.org/10.1093/gji/ggz168>.
- French, M., Zhu, W., Banker, J., 2016. Fault slip controlled by stress path and fluid pressurization rate. *Geophys. Res. Lett.* 43 (9), 4330–4339. <https://doi.org/10.1002/2016GL068893>.
- Giardini, D., 2009. Geothermal quake risk must be faced. *Nature* 462, 848–849. <https://doi.org/10.1038/462848a>.
- Goebel, T., Brodsky, E., 2018. The spatial footprint of injection wells in a global compilation of induced earthquake sequences. *Science* 361 (6405), 899–904. <https://doi.org/10.1126/science.aat5449>.
- Grigoli, F., Cesca, S., Rinaldi, A., Manconi, A., López-Comino, J., Clinton, J., et al., 2018. The November 2017 Mw 5.5 Pohang earthquake: A possible case of induced seismicity in South Korea. *Science* 360 (6392), 1003–1006. <https://doi.org/10.1126/science.aat2010>.
- Guérin-Marthe, S., Nielsen, S., Bird, R., Giani, S., Di Toro, G., 2019. Earthquake nucleation size: evidence of loading rate dependence in laboratory faults. *J. Geophys. Res., Solid Earth* 124 (1), 689–708. <https://doi.org/10.1029/2018JB016803>.
- Guglielmi, Y., Cappa, F., Lancon, H., Janowczyk, J., Rutqvist, J., Tsang, C., Wang, J., 2014. ISRM suggested method for step-rate injection method for fracture in-situ properties (SIMFIP): using a 3-components borehole deformation sensor. *Rock Mech. Rock Eng.* 47 (1), 303–311. <https://doi.org/10.1007/s00603-013-0517-1>.
- Guglielmi, Y., Cappa, F., Avouac, J., Henry, P., Elsworth, D., 2015a. Seismicity triggered by fluid injection-induced aseismic slip. *Science* 348 (6240), 1224–1226. <https://doi.org/10.1126/science.aab0476>.
- Guglielmi, Y., Elsworth, D., Cappa, F., Henry, P., Gout, C., Dick, P., Durand, J., 2015b. In situ observations on the coupling between hydraulic diffusivity and displacements during fault reactivation in shales. *J. Geophys. Res., Solid Earth* 120 (11), 7729–7748. <https://doi.org/10.1002/2015JB012158>.
- Hanks, T., Kanamori, H., 1979. A moment magnitude scale. *J. Geophys. Res., Solid Earth* 84 (B5), 2348–2350. <https://doi.org/10.1029/JB084iB05p02348>.
- Häring, M., Schanz, U., Ladner, F., Dyer, B., 2008. Characterisation of the Basel 1 enhanced geothermal system. *Geothermics* 37 (5), 469–495. <https://doi.org/10.1016/j.geothermics.2008.06.002>.
- Hauksson, E., Stock, J., Bilham, R., Boese, M., Chen, X., Fielding, E., et al., 2013. Report on the August 2012 Brawley earthquake swarm in Imperial Valley, Southern California. *Seismol. Res. Lett.* 84 (2), 177–189. <https://doi.org/10.1785/0220120169>.
- Healy, J., Rubey, W., Griggs, D., Raleigh, C., 1968. The Denver earthquakes. *Science* 161 (3848), 1301–1310. <https://doi.org/10.1126/science.161.3848.1301>.
- Hubbert, M.K., Rubey, W.W., 1959. Role of fluid pressure in mechanics of overthrust faulting. *Bull. Geol. Soc. Am.* 70 (2), 115–166. [https://doi.org/10.1130/0016-7606\(1959\)70\[115:ROFFPM\]2.0.CO;2](https://doi.org/10.1130/0016-7606(1959)70[115:ROFFPM]2.0.CO;2).
- Kammer, D., Radiguet, M., Ampuero, J., Molinari, J., 2015. Linear elastic fracture mechanics predicts the propagation distance of frictional slip. *Tribol. Lett.* 57 (3). <https://doi.org/10.1007/s11249-014-0451-8>.
- Kaneko, Y., Nielsen, S.B., Carpenter, B.M., 2016. The onset of laboratory earthquakes explained by nucleating rupture on a rate-and-state fault. *J. Geophys. Res., Solid Earth* 121 (6071–6091). <https://doi.org/10.1002/2016JB01314>.
- Ke, C.-Y., McLaskey, G., Kammer, D., 2018. Rupture termination in laboratory-generated earthquakes. *Geophys. Res. Lett.* 45 (23), 12,784–12,792. <https://doi.org/10.1029/2018GL080492>.
- Ke, C.-Y., McLaskey, G.C., Kammer, D.S., 2021. The earthquake arrest zone. *Geophys. J. Int.* 224, 581–589. <https://doi.org/10.1093/gji/ggaa386>.
- Keranen, K., Savage, H., Abers, G., Cochran, E., 2013. Potentially induced earthquakes in Oklahoma, USA: links between wastewater injection and the 2011 Mw 5.7 earthquake sequence. *Geology* 41 (6), 699–702. <https://doi.org/10.1130/G34045.1>.
- Keranen, K., Weingarten, M., Abers, G., Bekins, B., Ge, S., 2014. Sharp increase in central Oklahoma seismicity since 2008 induced by massive wastewater injection. *Science* 345 (448), 448–451. <https://doi.org/10.1126/science.1255802>.
- Kim, K., Ree, J., Kim, Y., Kim, S., Kang, S., Seo, W., 2018. Assessing whether the 2017 Mw5.4 Pohang earthquake in South Korea was an induced event. *Science* 360 (6392), 1007–1009. <https://doi.org/10.1126/science.aat6081>.
- Kranz, R., Frankel, A., Engelder, T., Scholz, C., 1979. The permeability of whole and jointed barre granite. *Int. J. Rock Mech. Min. Sci. Geomech. Abstr.* 16 (4), 225–234. [https://doi.org/10.1016/0148-9062\(79\)91197-5](https://doi.org/10.1016/0148-9062(79)91197-5).
- Kwiatek, G., Saarni, T., Ader, T., Bluemle, F., Bohnhoff, M., Chendorain, M., et al., 2019. Controlling fluid-induced seismicity during a 6.1-km-deep geothermal stimulation in Finland. *Sci. Adv.* 5 (5). <https://doi.org/10.1126/sciadv.aav7224>.
- Lu, X., 2009. Combined Experimental and Numerical Study of Spontaneous Dynamic Rupture on Frictional Interfaces. PhD dissertation. California Institute of Technology.
- Martínez-Garzón, P., Kwiatek, G., Sone, H., Bohnhoff, M., Dresen, G., Hartline, C., 2014. Spatiotemporal changes, faulting regimes, and source parameters of induced seismicity: a case study from the Geysers geothermal field. *J. Geophys. Res., Solid Earth* 119 (11), 8378–8396. <https://doi.org/10.1002/2014JB011385>.
- McLaskey, G., 2019. Earthquake initiation from laboratory observations and implications for foreshocks. *J. Geophys. Res., Solid Earth* 124 (12), 12882–12904. <https://doi.org/10.1029/2019JB018363>.
- McLaskey, G., Yamashita, F., 2017. Slow and fast ruptures on a laboratory fault controlled by loading characteristics. *J. Geophys. Res., Solid Earth* 122 (5), 3719–3738. <https://doi.org/10.1029/2019JB018363>.
- McLaskey, G., Lockner, D., Kilgore, B., Beeler, N., 2015. A robust calibration technique for acoustic emission systems based on momentum transfer from a ball drop. *Bull. Seismol. Soc. Am.* 105 (1), 257–271. <https://doi.org/10.1785/0120140170>.
- Neuzil, C., 1995. Abnormal pressures as hydrodynamic phenomena. *Am. J. Sci.* 295, 742–786. <https://doi.org/10.2475/ajs.295.6.742>.
- Nielsen, S., Taddeucci, J., Vinciguerra, S., 2010. Experimental observation of stick-slip instability fronts. *Geophys. J. Int.* 180 (2), 697–702. <https://doi.org/10.1111/j.1365-246X.2009.04444.x>.
- Noda, H., Nakatani, M., Hori, T., 2013. Large nucleation before large earthquakes is sometimes skipped due to cascade-up-implications from a rate and state simulation of faults with hierarchical asperities. *J. Geophys. Res., Solid Earth* 118 (6), 2924–2952. <https://doi.org/10.1002/jgrb.50211>.
- Noël, C., Passelègue, F., Giorgetti, C., Violay, M., 2019. Fault reactivation during fluid pressure oscillations: transition from stable to unstable slip. *J. Geophys. Res., Solid Earth* 124 (11), 10940–10953. <https://doi.org/10.1029/2019JB018517>.
- Passelègue, F., Brantut, N., Mitchell, T., 2018. Fault reactivation by fluid injection: controls from stress state and injection rate. *Geophys. Res. Lett.* 45 (23), 12,837–12,846. <https://doi.org/10.1029/2018GL080470>.
- Raleigh, C., Healy, J., Bredehoeft, J., 1976. An experiment in earthquake control at Rangely, Colorado. *Science* 191 (4233), 1230–1237. <https://doi.org/10.1126/science.191.4233.1230>.
- Rice, J., 1993. Spatio-temporal complexity of slip on a fault. *J. Geophys. Res.* 98 (B6), 9885–9907. <https://doi.org/10.1029/93JB00191>.
- Rubinstein, S., Cohen, G., Fineberg, J., 2007. Dynamics of precursors to frictional sliding. *Phys. Rev. Lett.* 98 (22). <https://doi.org/10.1103/PhysRevLett.98.226103>.
- Rutqvist, J., Stephansson, O., 2003. The role of hydrochemical coupling in fractured rock engineering. *Hydrogeol. J.* 11 (1), 7–40. <https://doi.org/10.1007/s10040-002-0241-5>.
- Scholz, C., 2002. *The Mechanics of Earthquakes and Faulting*, 2nd edition. Cambridge University Press.
- Scuderi, M., Collettini, C., 2016. The role of fluid pressure in induced vs. triggered seismicity: insights from rock deformation experiments on carbonates. *Sci. Rep.* 6 (24852). <https://doi.org/10.1038/srep24852>.
- Scuderi, M., Collettini, C., 2018. Fluid injection and the mechanics of frictional stability of shale-bearing faults. *J. Geophys. Res., Solid Earth* 123 (10), 8364–8384. <https://doi.org/10.1029/2018JB016084>.
- Scuderi, M., Collettini, C., Viti, C., Tinti, E., Marone, C., 2017. Evolution of shear fabric in granular fluid gouge from stable sliding to stick slip and implications for fault slip mode. *Geology* 45 (8), 731–734. <https://doi.org/10.1130/G39033.1>.
- Segall, P., Rice, J., 1995. Dilatancy, compaction, and slip instability of a fluid-infiltrated fault. *J. Geophys. Res.* 100 (B11). <https://doi.org/10.1029/95JB02403>.
- Shvarts, A., Yastrebov, V., 2018. Trapped fluid in contact interface. *J. Mech. Phys. Solids* 119, 140–162. <https://doi.org/10.1016/j.jmps.2018.06.016>.
- Uenishi, K., Rice, J.R., 2003. Universal nucleation length for slip-weakening rupture instability under nonuniform fault loading. *J. Geophys. Res.* 108 (B1), 2042. <https://doi.org/10.1029/2001JB001681>.
- Wei, S., Avouac, J., Hudnut, K., Donnellan, A., Parker, J., Graves, R., et al., 2015. The 2012 Brawley swarm triggered by injection-induced aseismic slip. *Earth Planet. Sci. Lett.* 422, 115–125. <https://doi.org/10.1016/j.epsl.2015.03.054>.
- Witherspoon, P., Wang, J., Iwai, K., Gale, J., 1980. Validity of cubic law for fluid flow in a deformable rock fracture. *Water Resour. Res.* 16 (6), 1016–1024. <https://doi.org/10.1029/WR016i006p01016>.
- Wu, B., McLaskey, G., 2019. Contained laboratory earthquakes ranging from slow to fast. *J. Geophys. Res., Solid Earth* 124 (10), 10270–10291. <https://doi.org/10.1029/2019JB017865>.
- Wynants-Morel, N., Cappa, F., De Barros, L., Ampuero, J., 2020. Stress perturbation from aseismic slip drives the seismic front during fluid injection in a permeable fault. *J. Geophys. Res., Solid Earth* 125 (7). <https://doi.org/10.1029/2019JB019179>.
- Ye, Z., Ghassemi, A., 2018. Injection-induced shear slip and permeability enhancement in granite fractures. *J. Geophys. Res., Solid Earth* 123 (10), 9009–9032. <https://doi.org/10.1029/2018JB016045>.
- Zastrow, M., 2019. South Korea accepts geothermal plant probably caused destructive quake. *Nature*. <https://doi.org/10.1038/d41586-019-00959-4>.